Nuclear Instruments and Methods in Physics Research A 615 (2010) 285–294

Contents lists available at ScienceDirect

Nuclear Instruments and Methods in Physics Research A

journal homepage: www.elsevier.com/locate/nima

Triple- and quadruple-escape peaks in HPGe detectors: Experimental observation and Monte Carlo simulation

N.L. Maidana [a,*], L. Brualla [b], V.R. Vanin [a], J.R.B. Oliveira [a], M.A. Rizzutto [a], E. do Nascimento [c], J.M. Fernández-Varea [c]

[a] Instituto de Física, Universidade de São Paulo, Travessa R 187, Cidade Universitária, CEP:05508-900 São Paulo, SP, Brazil
[b] NCTeam, Strahlenklinik, Universitätsklinikum Essen, Hufelandstr, 55, D-45122 Essen, Germany
[c] Facultat de Física (ECM and ICC), Universitat de Barcelona, Diagonal 647, E-08028 Barcelona, Spain

ARTICLE INFO

Article history:
Received 9 November 2009
Accepted 28 January 2010
Available online 2 February 2010

Keywords:
HPGe detector
Escape peaks
BGO detector
Coincidence measurements
Monte Carlo simulation

ABSTRACT

The triple- and quadruple-escape peaks of 6.128 MeV photons from the $^{19}F(p,\alpha\gamma)^{16}O$ nuclear reaction were observed in an HPGe detector. The experimental peak areas, measured in spectra projected with a restriction function that allows quantitative comparison of data from different multiplicities, are in reasonably good agreement with those predicted by Monte Carlo simulations done with the general-purpose radiation-transport code PENELOPE. The behaviour of the escape intensities was simulated for some gamma-ray energies and detector dimensions; the results obtained can be extended to other energies using an empirical function and statistical properties related to the phenomenon.

1. Introduction

Despite the increasing interest in the use of high-purity germanium (HPGe) detectors in the observation of high-energy gamma-rays, there is a lack of experimental work about their response for energies above ≈4 MeV. Older works [1,2] concentrate on the detector efficiency and rely on fitting a semi-empirical function with adjustable parameters to experimental values measured for photons in the range 59 keV–6.128 MeV obtained from radioactive sources. The high-energy interval can be accessed only with the help of photons generated in nuclear reactions, mainly proton- and neutron-capture reactions [3,4], and is being now explored by means of Monte Carlo (MC) simulation [5,6], which is also being applied to NaI(Tl) detectors [7]. Anyway, for photons above 4 MeV, no systematic experimental response function study was found in the literature.

During our work on the HPGe response function, we were faced with an interesting secondary detection effect: the third and fourth annihilation gamma-ray escape peaks. These peaks have the same nature as the well-known secondary detection effect that appears at energies above ≈2 MeV, which happens when the positron from the electron–positron pair formation annihilates with an electron, and the resulting 511 keV photons escape the detector volume. From the escape of one or two annihilation photons result the well-understood single- and double-escape peaks, denoted in what follows as SE and DE peaks, respectively. At higher energies, the $e^+ - e^-$ created by the incident photon have enough energy to yield bremsstrahlung photons with sufficient energy to produce a second electron–positron pair; when the formed positron annihilates, the resulting photons can escape. In what follows, the peaks formed by the escape of three and four annihilation gamma-rays will be called TE and QE peaks, respectively.

One of the MC codes used in the HPGe detector simulation pointed to a quite important TE intensity, which stimulated us to undertake its search in a simple experiment which, albeit unsuccessful [8], proved that the real intensity was much smaller than our first predictions. Afterwards, in a more detailed literature survey, we found that, although this phenomenon is not yet well described in the literature, the QE observation was indeed already reported by Wilkinson and Alburger [9], who came across it when searching for the double-pair formation by photons, in an experiment using 6.128 MeV gamma-rays from the same reaction as in the experiment described here, which was already briefly reported [10]. In Wilkinson and Alburger's experiment [9], however, the QE peak was barely visible, and the TE peak could not be seen.

In this paper, we report: the experiment that allowed the clear observation of the TE and QE peaks; the simulation of its production with the PENELOPE program; the general TE and QE properties; simulated values for some gamma-ray energies between 6 and 14 MeV and a few choices of detector sizes and

* Corresponding author. Tel.: +55 11 3091 6673; fax: +55 11 3091 6640.
E-mail address: nmaidana@if.usp.br (N.L. Maidana).

0168-9002/$ - see front matter © 2010 Elsevier B.V. All rights reserved.
doi:10.1016/j.nima.2010.01.073

aspect-ratios, as well as a formula that helps the interpolation between results. The consequences related to the possible measurement of the cross-section for double-pair formation by photons have been already discussed [10].

2. Experimental method

In order to observe the TE and QE peaks, a monochromatic photon source with high energy and intensity is required, which can be provided only by a nuclear reaction. We chose the $^{19}F(p,\alpha\gamma)^{16}O$ reaction, which was the same used by Wilkinson and Alburger [9]. The proton beam was provided by the 1.6 MV tandem accelerator of the Laboratory of Materials Analysis from the Instituto de Física, Universidade de São Paulo, LAMFI-USP. In the first observation trial, the TE and QE peaks were searched in singles spectra with a negative result, and an upper intensity limit was set [8]. Later, we performed both a coincidence experiment, which allowed their clear observation, and a singles spectrum measurement, as will be described in detail here.

2.1. Reaction and target

The $^{19}F(p,\alpha\gamma)^{16}O$ nuclear reaction was the photon source. The known level scheme of ^{16}O up to 7.2 MeV [11,12] is shown in Fig. 1, where the level half-lives are given.

In this reaction, the formed ^{20}Ne nucleus fissions in flight in an α- particle and a $^{16}O^*$ nucleus; hence, the recoiling excited $^{16}O^*$ nucleus can either stop in the target or leave it, when photons from the 6.1298, 6.9 and 7.1 MeV levels are emitted. The very short half-lives of 6.9 and 7.1 MeV $^{16}O^*$ excited levels result in large Doppler broadening of the detected gamma-rays, whereas in the case of the 6.1298 MeV level it can be brought to rest before photon emission. While the target is sufficiently thick to stop nuclei recoiling inward, those recoiling (from ^{20}Ne fission) in the opposite direction escape to the irradiation chamber and decay in flight, giving rise to a low-energy tail in the 6.128 MeV observed peak. In order to reduce this phenomenon, the targets, consisting of 150 $\mu g/cm^2$ CaF_2 evaporated on a 0.1-mm-thick Cu backing, were coated by 300 $\mu g/cm^2$ of evaporated Au to stop the $^{16}O^*$ recoils also in the backward direction.

Another target, consisting of 38 $\mu g/cm^2$ CaF_2 evaporated on 0.1-mm-thick Ta was built to determine the excitation function, as it will be explained in the next section.

The reaction used also feeds the $^{16}O^*$ 6.05 MeV excited state, which decays by internal pair formation and very small components of two-photon emission and internal conversion [11]. Absorbers were employed to avoid the detection of the high-energy electrons and positrons and the annihilation photons produced near the HPGe and BGO detectors, as will be described in Section 2.2.3.

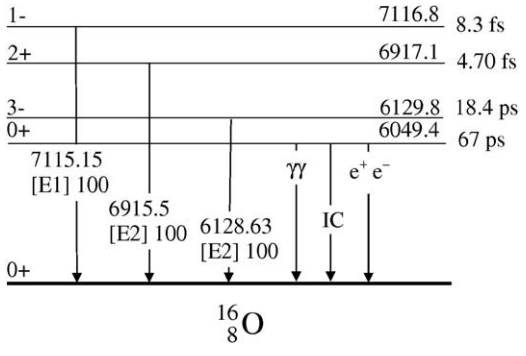

Fig. 1. Simplified ^{16}O level scheme [11,12]; energies in keV. Half-lives are given next to the level line.

2.2. Detection systems

The coincidence system consisted of a segmented annular scintillation BGO (bismuth germanate) detector and an HPGe detector positioned in its centre, hence the annihilation gamma-rays escaping from the HPGe detectors were observed in the annular detector; details on the coincidence detector arrangement, required by the calculations, are left for the simulation Section 4.1. The electronic circuit included a trigger to select out the events where at least two BGO segments fired. The singles spectrum was taken with another HPGe detector. Both the coincidence and the singles spectra were acquired simultaneously.

2.2.1. HPGe detectors

Two reverse-electrode closed-end coaxial HPGe detectors with 7.55 cm in diameter and 6.25 cm in length were used. The detector placed concentrically with the BGO detector had its axis aligned with the beam direction. The other was placed with its axis in a direction of about 90° relative to the beam direction, very close to the target, and was used both for measuring the excitation function (see Section 2.4) and accumulating a singles spectrum with the aim of observing the TE peak directly.

2.2.2. BGO detectors

The annular detector is formed by six independent BGO crystals, each one 19.85 cm in length and 3.0 cm thick, with a trapezoidal section measuring about 8.9 cm at the longest side, and covering a polar angle of nearly 60° around the axis of the mount. Since it is normally operated as Compton suppressor, the crystals have a 2.0 cm-thick extension protruding inwards 2.06 cm at the front, designed to detect photons backscattered in the HPGe crystal.

2.2.3. Collimator and absorbers

A collimator was specially designed for this experiment, in order to reduce the detection of 6 MeV primary reaction photons by the BGO detectors, without affecting the HPGe detection efficiency. It consisted of a block of Pb, $\approx$4 cm thick, with delimiting conical surfaces, so that the BGO-detector front side saw the target through its thickness, and the HPGe detector was not blocked from the reaction-produced photons.

To avoid the detection of electrons and positrons from the 6.05 MeV $^{16}O^*$ excited state and reduce the production of annihilation photons inside the detectors, we placed in front of the collimator a graded absorber made of Al, Cu, Cd and Pb.

2.3. Measurement setups

2.3.1. Singles spectrum

The singles spectrum was obtained with the HPGe detector positioned at 90° with respect to the beam using an ORTEC digital spectrometer, DSPEC. Pulse rise-time, RT, was set to 3.0 μs, flat-top to 1.6 μs, and the cusp parameter to 0.5; all these values but RT are equal to those chosen by the DSPEC automatic setup program, which indicated 7.0 μs for RT. The adopted values reduced the dead time to about 20% at the high counting rate obtained, $\approx$18 kHz in a spectrum dominated by 6–7 MeV photons, with an acceptable resolution. Fig. 2 displays the recorded singles spectrum.

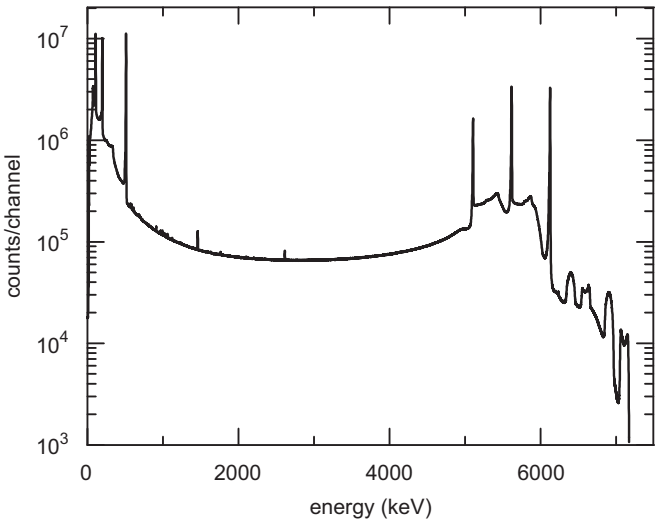

Fig. 2. Gamma-ray singles energy spectrum of $^{16}O^*$. The energy dispersion is 0.536 keV/channel.

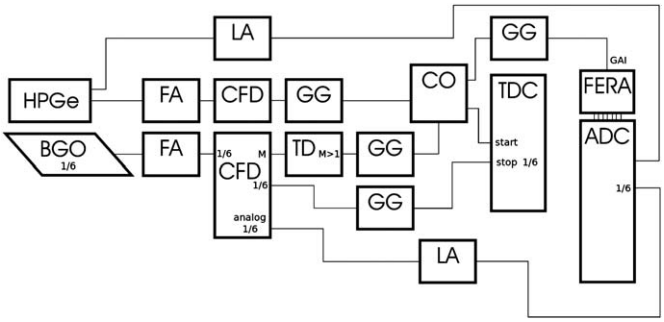

Fig. 3. Scheme of the pulse electronics setup. HPGe: high-purity Ge detector (Canberra) with pre-amp. BGO: one sector (out of 6) of the bismuth germanate detector (Cyberstar) with photomultiplier base. FA: fast amplifier (Ortec, Quad TFA 863). LA: linear amplifier with pile-up detection (Ortec, 572). CFD: constant fraction discriminator (Ortec, Octal CF8000). GG: gate generator (Ortec, Octal GG8010). TD: timing discriminator (Phillips Scientific, 710). CO: coincidence unit (LeCroy, 662). TDC: Camac time to digital converter (LeCroy, 2228A). FERA: Camac fast encoding and readout ADC driver (LeCroy, 4301). ADC: Camac analog to digital converter (Silena, 4418/V).

2.3.2. Coincidence spectra

Fig. 3 shows the electronics setup employed in the experiment. It is based on that used for Compton suppression with the BGO and HPGe detectors described here [13]. In this experiment, however, we have used a separate constant fraction discriminator for each of the six BGO segments in a single (Octal) CFD module. The multiplicity signal (M), formed by the superposition of the 200-ns-wide pulses of each CFD, is sent to a timing level discriminator (TD) where a minimum level is set corresponding to two or more coincident BGO segment pulses (i.e. within 200 ns). The coincidence of this signal with that from the HPGe detector is then verified in the coincidence module (CO) sending a logic pulse to the start of the TDC and opening the FERA gate for ADC acquisition. HPGe pulse pile-up was detected by the linear amplifier (LA), which provided the corresponding logic signal. The recorded event consisted of the energy deposited in each BGO (at least two of them), the time difference between the beginning signal of the HPGe and each BGO, the HPGe energy and the pile-up signal. The time resolution varied in the interval from 15 to 25 ns.

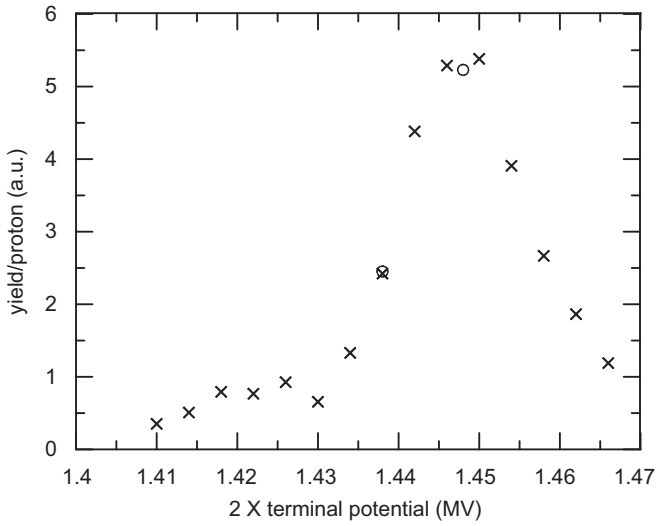

Fig. 4. Excitation function for a 38 μg/cm^2 CaF_2 evaporated on 0.1 mm-thick Ta in function of twice the nominal terminal voltage. The open circles at 1.438 and 1.448 MV were measurements done after all the other points, plotted as crosses, had been obtained, with the aim of verifying whether the terminal voltage measurements were reproducible.

2.4. Excitation function

The rate of production of the different photons from $^{16}O^*$ depends on the proton energy. We chose to excite the 1.378 MeV proton resonance, known to give a spectrum dominated by 6.128 MeV gamma-rays. To find precisely the correct beam energy, the excitation function for the target evaporated on Ta was used, because the Ta Coulomb excitation provided a simple method to compare the yields at different proton energies. Therefore, singles gamma spectra for different proton energies in short runs, with a terminal voltage producing protons close to 1.378 MeV, were measured with the HPGe detector at 90° with respect to the beam, with a current of ≈350 nA. Fig. 4 shows the ratio between the 6.128 MeV peak and the area of the 137 keV gamma-ray from Ta Coulomb excitation in the singles spectra, as a function of the terminal voltage.

2.5. Irradiation runs

Three CaF_2 targets covered with Au were irradiated. The appropriate terminal voltage was chosen for each one, determining a few points of another excitation function around a starting value equal to the peak of the function in Fig. 4 added to the expected proton energy loss in the Au deposit. After finding the appropriate terminal voltage, each target was irradiated for 1 day with about 200 nA current, which resulted in a count rate at the 6.128 MeV gamma-ray peak about 150 counts/s.

3. Experiment analysis

There were 2.6×10^8 coincidence events collected, including chance coincidences. These data were formed into HPGe gamma-ray spectra or coincidence matrices under selected coincidence requirements. We chose a time window for each BGO segment that included most of the true coincidence events, hence they were set in the range 60–80 ns, according to the resolution of the specific BGO detector. In the obtained data, chance coincidences had negligible effect in the escape peak areas and also in the selected matrices shown in this paper. For each event, the

multiplicity n was determined as the number of BGO segments that passed the time requirement.

All detectors—the HPGe and the six BGO segments—were calibrated in energy using the observed SE, DE and annihilation gamma-ray peaks, in appropriately gated true or chance coincidence spectra. The widths of the annihilation peak in the BGO segments were also determined, and varied from 49 to 62 keV, corresponding to $\approx 68\%$ of the peak area, determined in the BGO spectra in the n=2 coincidence fold gated by the DE peak in the HPGe spectrum.

Since the annihilation gamma-ray peak in the BGO spectra is Gaussian-shaped, we set a coincidence condition similar to that used for high-fold gamma-ray coincidence events [14], but that allows a precise evaluation of the fraction of events enclosed in the multidimensional gate. Then, for events of multiplicity n, the coincidence requirement is

$$\sum_{i=1}^{6}{}' \frac{(E_i - m_e c^2)^2}{\sigma_i^2} \le \chi^2_{\alpha,n} \tag{1}$$

where E_i and σ_i are the observed energy and width for the i-th BGO detector, respectively, corresponding to the simultaneous detection of n annihilation gamma-rays in the BGO segments. The prime in the summation symbol indicates that the sum must be restricted to the n terms that passed the time gate. The parameter $\chi^2_{\alpha,n}$ can be related to the fraction α of events in the multidimensional peak included in the gate. Since the BGO peak shape can be well approximated by a Gaussian, the fraction α of the peak area (for n=2), volume (n=3), or hyper-volume (n=4) can be evaluated from the cumulative distribution function of the χ^2-statistics for n degrees of freedom, where $\chi^2_{\alpha,n}$ is the critical value for the α percentage point.

Let us denote by A_{α_i} and s_i the peak area and associated standard deviation, respectively, for the n-escape peak in the HPGe gamma-ray spectrum obtained under the restriction imposed by formula (1) with a given α. From a set of values $\{A_{\alpha_i}, s_i, i = 1, \ldots, \mu\}$, it is possible to determine the expected total number of coincidence events, A, which would correspond to the ideal condition $\alpha = 100\%$, by the least-squares method. The linear model is $A_{\alpha_i} = \alpha_i A$, hence the design matrix $\mathbf{X}$ is given by $X_i = \alpha_i$. If all the peak areas are calculated with the same function, linear in the channel spectra counting numbers, then the variance matrix is given by

$$V_{ij} = \min\{s_i^2, s_j^2\} \tag{2}$$

because the gate formed with the bigger α contains all events in that formed with the smaller α. Using these design and variance matrices, along with the vector $\vec{A}_\alpha$ formed with the μ experimental values A_{α_i}, the least-squares solution for A, $\hat{A}$, is [15,16]

$$\hat{A} = (\mathbf{X}^t \mathbf{V}^{-1} \mathbf{X})^{-1} \mathbf{X}^t \mathbf{V}^{-1} \vec{A}_\alpha \tag{3}$$

with

$$\sigma_A^2 = (\mathbf{X}^t \mathbf{V}^{-1} \mathbf{X})^{-1} \tag{4}$$

and a goodness-of-fit test statistics can be calculated from the vector $\vec{D}$ of differences between the experimental and fitted peak areas defined such that $D_i = A_{\alpha_i} - \hat{A}$ by the formula

$$\chi^2 = \vec{D}^t \mathbf{V}^{-1} \vec{D} \tag{5}$$

which is distributed like χ^2 with $\mu - 1$ degrees of freedom. Note that, since the peak areas are strongly correlated, the precision in the fitted value is only slightly better than A_{α_i}/α_i for $\alpha_i \approx 0.9$. The real motivation for this procedure is that the χ^2 value allows the evaluation of the goodness-of-fit of this simple model and is an additional proof that the observed peak areas refer to the coincidence events that we are looking for.

4. Monte Carlo simulation

Monte Carlo simulations in the present article have been performed with the general-purpose radiation-transport code PENELOPE [17], which implements accurate physical interaction models (limited only by the required generality of the code) and a robust tracking algorithm for electrons, positrons and photons [18–20]. The PENELOPE subroutines were compiled with the main program `penmain` distributed with the code.

4.1. Simulation of the HPGe detector with an array of BGO detectors

The primary energy source was simulated as a plane of dimensions $0.2 \times 0.3\,\text{cm}^2$ emitting 6.128 MeV photons isotropically. The plane was centred and perpendicular to the main axis of the detection system, and in the same position that was actually placed in the experiment. The absorption energies (EABS), at which the track evolution is stopped and the energy of the particle is deposited locally, were set the same for all materials in the simulation of the HPGe crystal surrounded by an array of BGO detectors. The absorption energies were chosen to be 10 keV for electrons and positrons, and 1 keV for photons.

PENELOPE uses a mixed algorithm for the simulation of electrons and positrons, in which their interaction events are classified as hard or soft. Hard collisions are those involving angular deflections or energy losses above certain user-defined cutoffs. These events are simulated in a detailed way, that is, interaction-by-interaction. The combined effect of all soft events that occur between two hard collisions is simulated by means of an artificial single event. The PENELOPE transport parameters determine the average angular deflection between two consecutive hard elastic collisions (C_1), the maximum fractional energy loss between two hard elastic collisions (C_2), and the cutoff energy for hard inelastic interactions and hard bremsstrahlung emission (W_{cc} and W_{cr}, respectively) [17]. The simulation parameters were set to: energy-loss cutoff values W_{cc} and W_{cr} equal to 1 keV, multiple-scattering parameters $C_1 = C_2 = 0.05$. Parameter DSMAX determines the maximum allowed step length for electrons and positrons. In order to limit the step length, the code places delta interactions along the track of a particle. The value of DSMAX for each thin body encountered along the beam path has been set equal to one tenth of the thickness of each of those bodies.

The geometrical models of the simulated detectors were done with the code PENGEOM which allows to build objects by grouping quadric surfaces. In the case of the HPGe detector surrounded by the hexagonal array of BGO detectors, the dimensions given by the manufacturer were followed, including the thicknesses of the HPGe dead layers. The HPGe crystal was modelled as a cylinder 7.55 cm in diameter and 6.25 cm in length, with an internal cylindrical hole for the cold finger, of diameter 0.75 cm and length 4.85 cm. The Pb collimator and the absorbing foils in front of it were also modelled. Fig. 5 displays a three-dimensional image of the arrangement, in which a wedge has been excluded to allow vision of the inner parts of the detection system. The graded absorbers placed to prevent detection of high-energy electrons and positrons from the decay of $^{16}O^*$ correspond to materials Al (1), Cu (2), Cd (3) and Pb (4), with thicknesses of 1.10, 0.67, 1.36 and 0.27 mm, respectively. The special Pb collimator is labelled with number (5) and the BGO detector segments with number (6). The BGO and HPGe end caps were simulated as a single Al cylinder with thickness equal to 3.75 mm. This thickness amounts to the added thicknesses of both end caps. The Al cylinder had a frontal centred hole that was covered by a Be window of thickness and diameter set according to the instructions of the manufacturer.

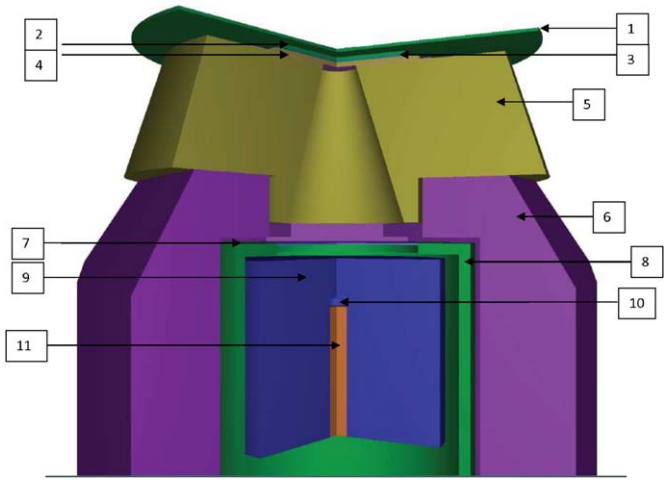

Fig. 5. Three-dimensional image of the detectors used by the simulation program. Only part of the BGO detectors are shown since they extend downwards about 10 cm more. In the figure a wedge has been excluded to reveal the inner structure of the detection system.

4.1.1. HPGe detector operating in coincidence with the BGO detectors

For the cases in which a logic of coincidences has been used, `penmain` was modified in order to incorporate these logical schemes. Each BGO crystal was defined in the simulation as an energy-deposition detector. The energy deposited in each BGO detector by a given shower is referred to as e_i, with $i=\{1,\ldots,6\}$ a label that identifies each BGO detector. The HPGe crystal was also defined as an energy-deposition detector. The energy deposited during a given shower in the HPGe crystal is referred to as E_{HPGe}.

In order to implement the Gaussian broadening characteristic of BGO detectors, the energy deposited in each BGO detector after completing a shower was stochastically modified according to the following model:

$$\tilde{e}_i^2=\left[\frac{(e_i-\xi\,\overline{\sigma})-m_e c^2}{\overline{\sigma}}\right]^2 \quad \forall i=\{1,\ldots,6\} \tag{6}$$

where $\overline{\sigma}=54$ keV is the average width of the annihilation peak of the six BGO detectors, and ξ is a normally distributed random number.

For evaluating the fraction α of the peak area (for n=2), volume (n=3), or hyper-volume (n=4) the following conditional statements were used after completing each shower (see Eq. (1))

$$\text{if } \tilde{e}_i^2+\tilde{e}_j^2 \overset{\forall i,j=\{1,\ldots,6\}}{\underset{i<j}{\leq}} 5.99 \quad \text{then } f\leftarrow \texttt{TRUE} \tag{7}$$

$$\text{if } \tilde{e}_i^2+\tilde{e}_j^2+\tilde{e}_k^2 \overset{\forall i,j,k=\{1,\ldots,6\}}{\underset{i<j<k}{\leq}} 7.81 \quad \text{then } f\leftarrow \texttt{TRUE} \tag{8}$$

$$\text{if } \tilde{e}_i^2+\tilde{e}_j^2+\tilde{e}_k^2+\tilde{e}_l^2 \overset{\forall i,j,k,l=\{1,\ldots,6\}}{\underset{i<j<k<l}{\leq}} 9.49 \quad \text{then } f\leftarrow \texttt{TRUE} \tag{9}$$

in which conditional statements (7)–(9) correspond to the cases n=2, 3 and 4, respectively. The values 5.99, 7.81 and 9.49 were obtained from $\chi^2_{\alpha,n}$ tables using $\alpha=95\%$ and the corresponding n. The appearance of a coincidence is denoted through the logical variable f, initialised to `FALSE` at the beginning of each shower. Independent simulations were run in order to take into account each of the considered cases described in the conditional statements (7)–(9).

At the end of each shower the energy deposited in the HPGe detector (E_{HPGe}) was set to zero if f=`FALSE` or left unaltered if f=`TRUE`. Finally, the value stored in E_{HPGe} was transferred to a cumulative variable.

4.1.2. Simulation of the HPGe detector with modified dead layers

As it will be explained below, the simulation of the whole spectrum obtained from the HPGe detector in presence of the BGO array and collimator, without taking into account the coincidence logic, yielded an SE/DE peak intensity ratio different from the experimental result. This discrepancy can be, in part, due to the presence of a semi-dead layer around the cold finger dead layer, as it has been suggested by Utsunomiya et al. [5]. This possibility was investigated by simulation, resorting to a model similar to that described by these authors.

According to the HPGe detector manufacturer specifications, there is a dead layer around and on top of the cold finger whose thickness amounts to 0.5 mm. This dead layer has been included in all simulations related to the HPGe detector. In order to simulate the HPGe detector with the dead layer, the volume of the HPGe crystal was divided into different bodies. One body represented the active part of the detector where an energy-deposition detector was defined, and the other body was defined as the dead layer in which the energy deposited was not tallied.

The model for charge collection efficiency introduced by Utsunomiya et al. was implemented in the following way. A transition region of thickness 1 mm around and on top of the dead layer surrounding the cold finger was defined as a separate body. If a particle were to deposit energy in that region its distance x to the dead layer was determined. A scoring probability was defined according to

$$\mathcal{P}(x)=1-\exp(-x/d_n) \tag{10}$$

where d_n=0.1 mm is a characteristic distance extracted from the work of Utsunomiya et al. Then $\mathcal{P}(x)$ was compared to a uniformly distributed random number ζ. If $\mathcal{P}(x)\geq\zeta$ the energy deposited in the transition region was transferred to the energy-deposition detector defined in the HPGe. If $\mathcal{P}(x)<\zeta$ the energy deposited in the transition region was zeroed. It can be seen that this algorithm tends to tally no energy as the contributing particle approaches the dead layer, and tends to tally all energies as the contributing particle approaches the active scoring volume of the HPGe.

4.2. Simulation of ideal Ge detectors

To obtain the TE/DE ratio we simulated three ideal detectors consisting of cylindrical Ge crystals with a volume of 5 cm^3 with dimensions 5 cm^2 frontal area $\times$1 cm length; 71 cm^3 with dimensions 15.8 cm^2 frontal area $\times$4.5 cm length, and 280 cm^3 with dimensions 44.8 cm^2 frontal area $\times$6.25 cm length. In order to consider the effect of the aspect ratio of the detector on the escape peak ratios, the 71 cm^3 ideal detector was considered with three different aspect ratios with one of the energy sources, namely 1:1 (length 4.5 cm, diameter 4.5 cm), 2:3 (length 3.425 cm, diameter 5.136 cm) and 3:2 (length 5.881 cm, diameter 3.92 cm). The simulated isotropic point source of monoenergetic photons was placed in the longitudinal axis at 10 cm from the crystal surface, in vacuum. For studying the energy dependence of the TE/DE rate, six different primary energies were considered, ranging from 4 to 14 MeV photons in steps of 2 MeV. We made some additional simulations for the 5 cm^3 crystal and 14 MeV photon energy to calculate the dependence of the TE/DE rate for other distances, namely 5 and 20 cm from the crystal surface. In all cases, the whole HPGe crystal was defined as an energy-deposition detector. The absorption energies of electrons and positrons were set to 100 keV, and those of photons to 10 keV. The

simulation parameters were set to W_{cc}=1 keV, W_{cr}=10 keV and C_1=C_2=0.05.

5. Results

We first present the experimental results on the intensities of the QE and TE peaks, which were observed in folds $2 \le n \le 4$ and barely seen in the singles spectrum, and compare them with the simulation results. After that, we explain why in this particular experimental arrangement a clear observation of the photons from bremsstrahlung in the Ge crystal was impossible, despite the neat observation of the annihilation escape peaks that depend on the emission of bremsstrahlung. Next we point out the relationship between the QE/TE ratio and the DE/SE ratio, which turns out to be a signature of this secondary detection phenomenon and can be deduced from basic statistical properties of the detection process. Then, we show the predicted behaviour of the TE and QE peaks with detector volume, dimensions, photon energy and source-to-detector distance; about the last one we will just report that it was not found any evidence that the escape ratios depend on the distance to the source.

5.1. Experimental intensities of escape peaks

We formed HPGe detector spectra from coincidence events with n=2, 3, or 4 BGO segments under the restriction expressed by expression (1) with $0.1 \le \alpha \le 0.9$ in steps of 0.1, $\alpha = 0.95$ and 0.99. Fig. 6 presents the TE and QE peaks in selected spectra with different values of α. As illustrated by the figure, in some cases the shape of the continuum component around the peak changes with varying α, with the result that the fitting procedure has to change from spectrum to spectrum and the variance matrix between the peak areas of formula (2) is no more strictly valid. Although the peak area data sets, when fitted by the least squares method (formulas (2)–(5)) resulted in χ^2- values that fell well in the acceptance region, we decided to adopt a fixed procedure to determine peak areas to avoid any unforeseen errors induced by the approximated variance matrix. Therefore, TE and QE intensities in n=3 spectrum and the DE intensity in n=2 were taken from the spectra for $\alpha = 0.95$, while total numbers of coincidences for TE in n=2 spectra and QE in n=4 spectra were determined using the fit procedure, and the result was downscaled to 95%.

Since the TE and QE peaks are not prominent and should be distorted because they are originated by reaction photons sometimes emitted in flight, the procedure for the determination of their area was chosen from the DE peak, which is expected to be similar in shape. The positions of the escape peaks were determined from the detector energy calibration. The objective procedure consisted of summing the number of counts of the four channels to the right and eight channels to the left of the expected peak position and subtracting the numbers of counts from six channels to the right and six more to the left in blocks displaced of six and 10 channels, respectively, relative to the expected peak position. Fig. 7 shows the results for the QE peak in n=4 spectrum and TE peak in n=2 along with the fitted values given by the expected total number of coincidence events from Eq. (3), which are the cases where the continuum component of the energy spectrum can be well approximated by a straight line around the peak for all α.

In Table 1 we quote the ratios of experimental QE and TE intensities in the HPGe spectrum with n=2, 3, 4 to the DE intensity in n=2, using the peak areas obtained as explained in the previous paragraphs, compared to the corresponding simulated values, whose quoted standard deviations refer to MC statistical

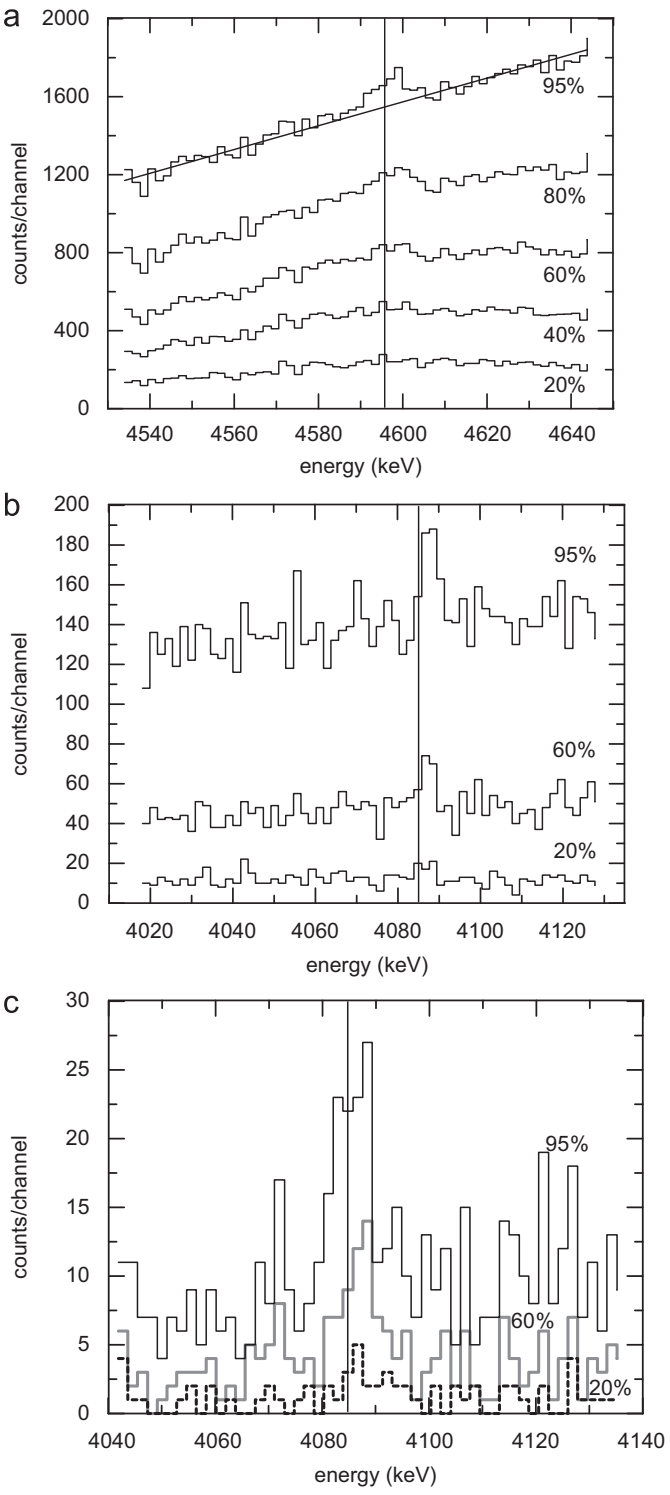

Fig. 6. Regions of interest in coincidence spectra under the restriction (1) with selected α- percentage points: (a) TE in fold n=3; (b) and (c) QE in folds n=3 and n=4, respectively. The dispersion is 1.83 keV/channel.

fluctuation only. Notice that these ratios were calculated from peak areas pertaining to different coincidence folds, and are not the expected ratios in singles spectra; even when the TE and DE peak areas were measured in the same fold n=2, its ratio is not equal to that of the singles spectrum, because the BGO coincidence system detection efficiency for two of two annihilation photons (DE condition) is different from that for two of three annihilation photons (TE condition).

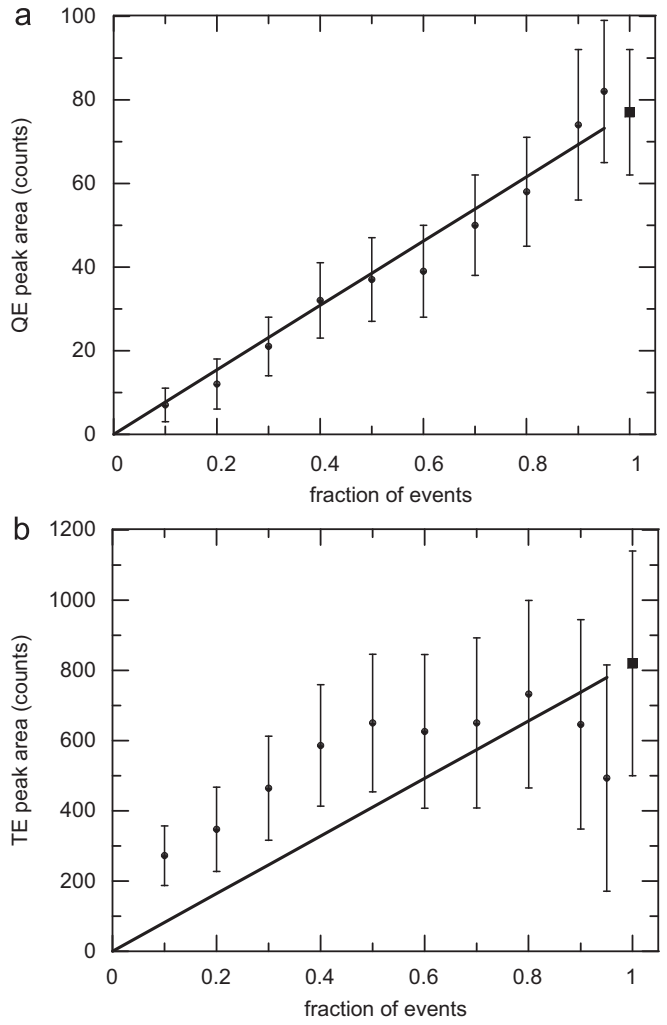

Fig. 7. (a) QE peak area in n=4 and (b) TE peak area in n=2 coincidence spectra under the restriction (1) with different α- percentage points and the corresponding fitted model, represented by the line and the point with uncertainty bar at fraction 100%. Notice that the experimental values are strongly correlated and the model function requires that the line intersects the origin.

Table 1
Ratios between peak areas in the spectra recorded in coincidence with different multiplicities n and the DE peak recorded with n=2. The numbers parentheses are uncertainties (one standard deviation), given in units of the value's last digit.

n	$10^5 \times$ QE/DE		$10^4 \times$ TE/DE	
	Exp	MC	Exp	MC
4	1.7 (3)	1.54 (14)		
3	3.0 (14)	3.1 (3)	1.6 (5)	1.39 (8)
2			1.8 (7)	2.34 (15)

The result obtained with the singles spectrum, where the TE peak is near the detection threshold, is given in Table 2 and compared with the simulated value, along with the experimental and simulated values for the SE/DE ratio. The latter quantity can be measured quite precisely and disagrees with the simulated values when the small uncertainty bars are considered. In Section 6, the possible solutions for this difference will be discussed and it will be shown that, with the present knowledge on HPGe detector characteristics, an additional 30% must be added to the statistical standard deviations reported for the MC simulated values to account for systematic uncertainties, as explained in Section 6.3.

5.2. Detection of bremsstrahlung photons escaping the HPGe detector

Electron or positron bremsstrahlung occurs in almost all HPGe gamma-ray detection events, but most of the ensuing photons have very low energies; hence, they deposit all the energy by photoelectric effect very near their production place and do not give rise to any measurable effect. However, those photons with enough energy to escape the HPGe detector can fire the BGO detectors. A bremsstrahlung photon generated inside the detector has a maximum escaping probability around a few hundreds of keV because, for a given electron energy, the decrease in bremsstrahlung photon intensity spectrum with energy is counterbalanced by the increased escaping probability at higher photon energy.

Fig. 8 depicts the level curves of a matrix built to observe, in the BGO detector, bremsstrahlung photons generated by the particles created from a pair-formation photon interaction inside the HPGe detector, using only events of multiplicity n=3. The energy observed in the HPGe is in the horizontal axis, while in the vertical axis is the energy of one of the n=3 BGO segments, chosen at random, on the condition that the energies observed in the other two BGO segments follow the requirement expressed by Eq. (1) with $n'=2$ annihilation photons and $\alpha=0.5$. The large peak around 4.6 MeV in the HPGe and 0.5 MeV in the BGO can be assigned to annihilation photons in coincidence with the continuum component of the energy spectrum under the $n'=2$

Table 2
Ratios between peak areas in the singles spectrum.

$10^4 \times$ TE/DE		SE/DE	
Exp	MC	Exp	MC
2.6 (15)	3.5 (12)	2.00 (3)	2.68 (1)

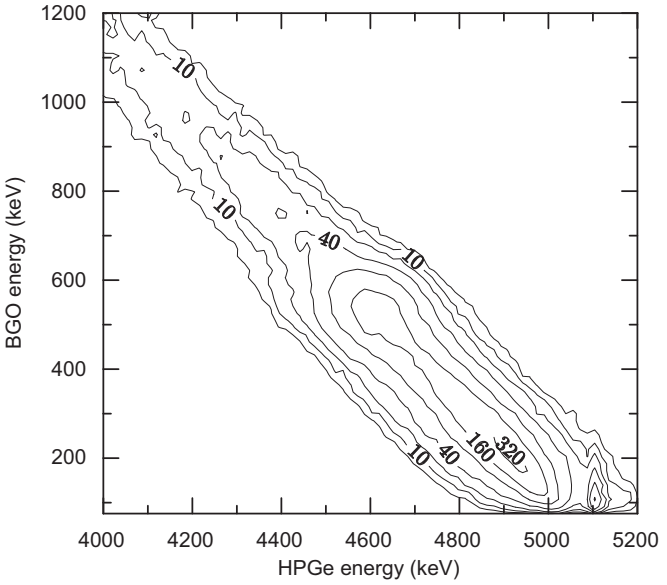

Fig. 8. Contour lines in the BGO vs HPGe energy matrix in fold n=3, requiring that $n'=2$ BGO segments fired with annihilation photons. The contour-lines were drawn in a $\log_2$ scale, beginning at 5 counts, and only the 10, 40, 160, and 320 count contour lines were labelled.

two-dimensional peak around m_ec^2 for both BGO segments included in the gate condition (1). Another possible procedure to build a matrix to get the same information, which consists in accepting events for each segment where the other two segments passed requirement (1) with $n'=2$, reinforces this structure by placing three times the events where all segments observed photons with energies near m_ec^2, while choosing the two segments with energies closer to m_ec^2 to pass gate requirement (1), produces a hole in this energy region, since there is a bias against events near m_ec^2. The events that have made this experiment difficult, obfuscating the TE peak in every spectrum build for its observation (a closer look into the data used to build Fig. 8 also shows traces of the TE peak, too blurred by the underlying structure to be useful), are in the large structure which peaks around 4.9 MeV and extends to <4 MeV in the HPGe. One of the processes that contributes to this ridge is the detection of the bremsstrahlung photon in coincidence with two annihilation photons detected in the other two BGO segments. Note that when a photon with energy E_b escapes from the HPGe detector and two annihilation photons are detected in BGO segments, the energy deposited in the HPGe is 6.128 MeV $-2m_ec^2-E_b$.

However, a simulation study, where the bremsstrahlung photon escaping the HPGe detector was tagged, revealed that only $\approx 1/3$ of this large bump is due to bremsstrahlung photons that were detected by the BGO. The remaining 2/3 are events generated by small-angle scattering of the 6.128 MeV gamma-ray in the BGO crystal extension at its front (Fig. 5): in the BGO nose, the recoiling electron deposits some hundreds of keV, and the photon is eventually detected in the HPGe by pair formation. Therefore, this event has exactly the same detection characteristics of the bremsstrahlung or the TE peak and we could not devise any gate condition to exclude them. A clear observation of the bremsstrahlung photons requires, as a consequence, to change the shape of the detector used to observe the annihilation photons or a much thicker collimator to shield the BGO from the high-energy photons.

5.3. TE dependence on detector size and energy

In order to understand the behaviour of the TE and QE peaks with detector size and photon energy, ideal detectors were simulated as explained in Section 4.2 for photon sources in the range 4–14 MeV. Table 3 and Fig. 9 summarize the results for the TE/DE intensity ratios for the different detectors; results for 4 MeV photons were omitted because they were not statistically meaningful. A close inspection shows that the TE/DE intensity ratio behaves as the 4th power of the energy; hence, it can be estimated in the energy range $6\,\text{MeV} \le E_\gamma \le 14\,\text{MeV}$ by the function

$$\left.\frac{\text{TE}}{\text{DE}}\right|_{E_\gamma} = \left.\frac{\text{TE}}{\text{DE}}\right|_{E_\gamma = 10\,\text{MeV}} \left(\frac{E_\gamma}{10\,\text{MeV}}\right)^4. \quad (11)$$

Table 3
Simulated triple to double escape intensity ratios, multiplied by 10^3, in singles spectra for ideal cylindrical HPGe detectors and several photon energies, E_γ. The quoted statistical uncertainties correspond to one standard deviation.

E_γ (MeV)	$10^3 \times$ TE/DE		
	5 cm^3	71 cm^3	280 cm^3
6	0.029 (21)	0.209 (11)	0.38 (5)
8	0.14 (3)	0.891 (14)	1.28 (10)
10	0.25 (10)	2.476 (21)	3.85 (14)
12	0.71 (16)	5.24 (3)	8.48 (22)
14	1.55 (26)	9.38 (5)	14.5 (3)

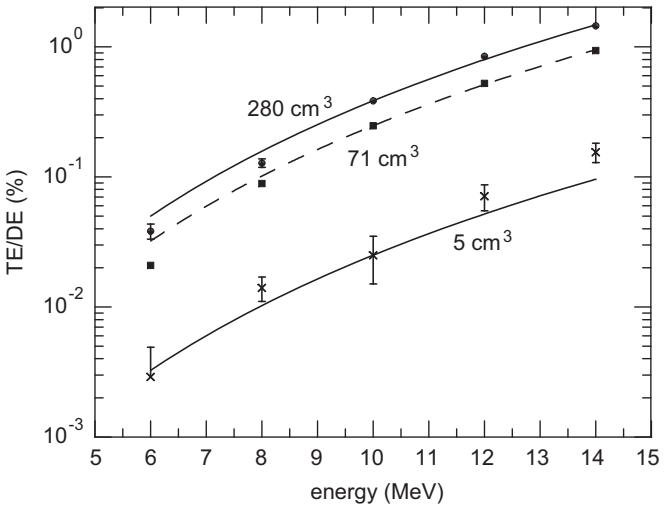

Fig. 9. Simulated TE/DE intensity ratio as a function of photon energy for ideal cylindrical HPGe detectors of the indicated active volumes. The uncertainty bars correspond to one standard deviation in the simulation statistics. The curves correspond to Eq. (11), which extrapolates the ratio for E_γ=10 MeV to all energies as a simple power law.

Table 4
Simulated QE/DE ratios in the singles spectra for ideal cylindrical HPGe detectors. The values were multiplied by 10^3 and the quoted uncertainties correspond to one standard deviation.

E_γ (MeV)	$10^3 \times$ QE/DE		
	5 cm^3	71 cm^3	280 cm^3
6	0.021 (19)	0.112 (9)	0.06 (4)
8	0.47 (3)	0.470 (12)	0.27 (8)
10	1.24 (10)	1.274 (17)	0.58 (10)
12	2.67 (16)	2.601 (26)	1.29 (15)
14	4.9 (3)	4.58 (4)	2.61 (22)

Using the intensity ratios for 10 MeV from Table 3 in formula (11), the TE/DE ratio for 280 and 71 cm^3 detectors can be estimated within uncertainty bars in the range 8–14 MeV and, less precisely, within a factor smaller than two, for the 5 cm^3 detector and the other detectors at 6 MeV. The QE/DE ratio, whose simulated values are listed in Table 4, can also be determined from the TE/DE ratio by another relation, which will be deduced in Section 5.5.

5.4. Dependence of the escape peak intensities on detector crystal aspect ratio

A typical HPGe gamma-ray detector crystal is a cylinder with a length L similar to its diameter D. We investigated how the aspect ratio L/D affects the escape peak intensities simulating the detection of 14 MeV photons by 71 cm^3 detectors of three aspect ratios, namely L/D= 2/3, 1 and 3/2.

The results are given in Table 5, where an increase in the TE and QE intensities can be observed when L/D increases. Since both pair creation and electron bremsstrahlung are forward-peaked processes (i.e. whose differential cross-sections are largest in the forward direction), the sequential double pair formation is enhanced in a lengthier detector. On the other hand, SE/DE and FE/DE ratios, where FE stands for the full-energy absorption peak, do not change so much with the aspect ratio, because they depend on the interaction of the annihilation gamma-rays, distributed isotropically.

Table 5
Simulated escape and full energy absorption peak (FE) intensity ratios in singles spectra for ideal cylindrical 71 cm^3 HPGe detectors of different length to diameter, L/D, ratios. A source of 14 MeV photons was placed 10 cm from the detector on its symmetry axis. The quoted statistical uncertainties correspond to one standard deviation.

Ratio	L/D		
	2/3	1	3/2
SE/DE	1.0527 (5)	1.0771 (5)	0.9763 (5)
FE/DE	0.31006 (21)	0.32454 (21)	0.28647 (20)
TE/DE	0.00834 (5)	0.00938 (5)	0.01006 (5)
QE/DE	0.00414 (4)	0.00458 (4)	0.00527 (4)

5.5. Relation between QE/TE and DE/SE

Let us denote by p and q the probabilities that an annihilation photon escapes from the sensitive volume of the detector without interaction and interacting with partial energy loss, respectively; hence, $1-p-q$ is the probability that an annihilation photon deposits all its energy inside the detector active volume. Now, we use σ_π and $\sigma_{\pi\pi}$ to denote the number of detection events originated from the primary photon by single and sequential double pair creation processes, respectively. Since $\sigma_{\pi\pi} \ll \sigma_\pi$, the DE and SE peak areas are well approximated by $DE \cong \sigma_\pi p^2$ and $SE \cong 2\sigma_\pi p(1-p-q)$, respectively. In order to develop analogous formulas for the QE and TE peak areas, we extend these formulas to any number of annihilation photons, assuming that the escape probabilities p and q do not depend on the process producing the annihilation photons in the detection event.

The probability that, from a total of M annihilation photons, a number n of them escape the detector active volume without any energy deposition, while the remaining photons deposit all their energy, is given by the multinomial probability function where the number of annihilation photons interacting within the detector and depositing part of their energies is set to 0

$$P_M(n) = \binom{M}{n} p^n (1-p-q)^{M-n}. \tag{12}$$

The QE/TE ratio can be calculated from expression (12) with M=4 and the number of primary events, $\sigma_{\pi\pi}$:

$$\frac{QE}{TE} = \frac{\sigma_{\pi\pi} P_M(M)}{\sigma_{\pi\pi} P_M(M-1)} = \frac{1}{4}\,\frac{p}{1-p-q}. \tag{13}$$

In turn, the DE/SE ratio can be calculated from expression (12) with M=2 and the number of primary events, σ_π:

$$\frac{DE}{SE} = \frac{\sigma_\pi P_M(M)}{\sigma_\pi P_M(M-1)} = \frac{1}{2}\,\frac{p}{1-p-q}. \tag{14}$$

Therefore,

$$\frac{QE}{TE} = \frac{1}{2}\,\frac{DE}{SE}. \tag{15}$$

This result is in agreement with the outcome of the simulations. Since the annihilation photons from the sequential double pair creation process are formed, on average, in a deeper detector region, it was expected to observe some departure from this law with the simulated process in the small detectors. However, even in the case of the small 5 cm^3 detector, the obtained results agree with relation (15) within uncertainties.

6. Discussion

Table 2 shows that the precise experimental SE/DE ratio does not agree with the simulated value. From Eq. (14), it is seen that this ratio depends only on the tracking of the annihilation photon histories inside the detector, and not on the pair-formation total cross-section. It is known that a fine tuning of the simulated efficiencies demands changes in the internal detector dimensions because there is a lack of information on internal parameters of the HPGe detector (e.g. the dimensions of dead layers), not always in agreement with the manufacturer's specifications [21].

From expression (14), which states that SE/DE is proportional to the ratio of annihilation photon total absorption probability to annihilation photon escape without any energy loss probability, it is seen that the overestimation of SE/DE ratio follows from the overestimation of the total absorption probability. Therefore, it is possible to fit the experimental SE/DE ratio increasing the detector dead layer thicknesses, which increases the possibility of partial photon energy absorption, and Ge crystal radius and length, which affect the interaction probability. However, we found that only too radical changes in these dimensions would lead to results in agreement with the experiment, which prompted us to search for other explanations.

6.1. Search for positron annihilation by three photons

The possibility of a process leading to a peak in $E_\gamma - 2m_ec^2$ but not to a peak in $E_\gamma - m_ec^2$ was considered. Although positron annihilation with the creation of three photons is an unlikely outcome, it is capable to contribute events to the peak at $E_\gamma - 2m_ec^2$ when all annihilation photons escape the detector, but it cannot add events to the peak at $E_\gamma - m_ec^2$, because the $2m_ec^2$ positron plus electron rest energy is distributed continuously among the three annihilation photons, hence the absorption of one or two of these annihilation photons do not peak at m_ec^2.

While it is known that the ratio of three photons creation to two photon events in electron–positron annihilation is $\approx 1/380$ or less [22,23], there was a suggestion that this phenomenon could be important in the HPGe detector response function [24], and it would lead to an enhancement in the observed DE intensity over the SE. Since this experiment is well suited for the search of electron–positron annihilation with three photons creation, we analyzed our coincidence data to check if, by any chance, the particular environment of the Ge crystal detector could enhance the three-photon branch.

The annihilation of a positron with the emission of three photons most likely leads to photons with similar energies, in coplanar directions forming angles near 120°. Therefore, we generated a two-dimensional BGO-BGO energies matrix, submitted to the conditions: fold n=3, detection in non-neighbouring BGO segments, and DE in the HPGe. Fig. 10 shows the obtained matrix. It can be seen that the energy region where the triple-photon annihilation events are expected is empty, and the coincidences are dominated by events where one of the annihilation photons is detected in the FE peak and the other is detected by inelastic scattering with the scattered photon escaping the HPGe but being detected in the third BGO segment. Although it is difficult to place a precise upper limit for the triple-photon annihilation intensity, considering that only a few percent of the DE peak is in fold n=3 and the peak to valley ratio in Fig. 10 is about 1/10, it can be conservatively set to $< 10^{-2}$ events per positron annihilation, ruling out this explanation for the DE peak enhancement.

6.2. Incomplete charge collection in the HPGe detector

Utsonomiya et al. [5] observed that some of the detection events where the photon deposits all its energy inside the detector active volume are not counted in the FE peak due to the draining of electrons from the conduction band by surface

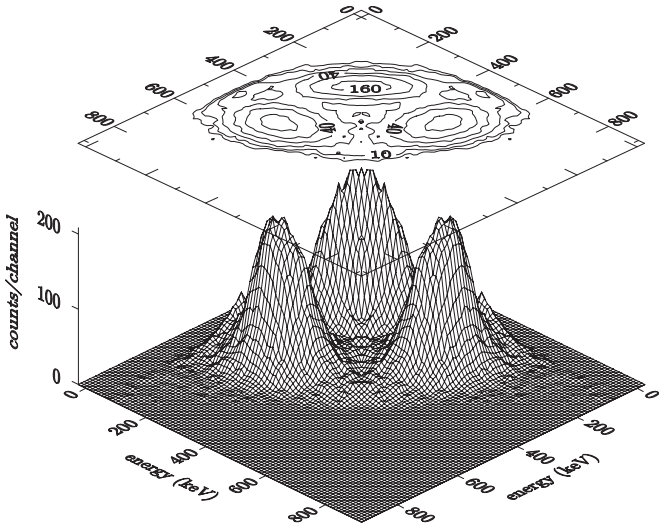

Fig. 10. Contour lines in the BGO-BGO energy spectrum in fold n=3, with the condition that the HPGe observed the 6.128 MeV photon DE peak and three non-neighbouring BGO segments were fired. The contour lines were drawn in a $\log_2$ scale, beginning at 5 counts, and only the 10, 40, and 160 count contour lines were labelled.

channels which affects the electron mobility to the point where they are collected much later than the other electrons in the pulse, leading to incomplete charge collection events that are not treated in the simulation program. In the specific experiment reported by Utsonomiya et al., this effect can affect the FE peak at low energy in as much as 20%, which is comparable to the difference between experiment and simulation in SE/DE ratio observed here. Using the algorithm described in Section 4.1.2, the simulated SE/DE ratio is reduced by about 4%, which suggests that it may be possible to fit, with reasonable changes in the semi-dead layer, the experimental result without altering the other ratios.

6.3. Evaluation of the systematic errors

It was found that the experimental SE/DE ratio can be fitted with changes in detector dimensions combined with an empirical model for incomplete charge collection. However, there are many sets of detector dimensions and model parameters that fit our experimental result. Moreover, there are other known effects that result in incomplete charge collection [25] and should be taken into account. The detailed study of this subject requires many other experimental data, and it is beyond the scope of the present article. Therefore, despite the good agreement between experiment and simulated data listed in Table 1, we will assign an additional 30% of systematic error in the simulated values, which is the difference found between experiment and simulation in the SE/DE ratio given in Table 2, and propagates to TE/DE and QE/DE ratio, as already discussed in detail by Maidana et al. [10].

7. Conclusion

We observed a secondary detection effect of high-energy gamma-rays with energy E_γ in HPGe detectors, which is the formation of peaks at energies $E_i \cong E_\gamma - im_ec^2$ with i=3, 4 and where m_ec^2 is the electron rest energy, approximately equal to the annihilation photon energy, arising from multiple e^+-e^- pair formation in a cascade process. The third- and fourth-order escape peaks were called Triple Escape (TE) and Quadruple Escape (QE) peaks, respectively; in an extension of the common names Single Escape (SE) and Double Escape (DE) for the first and second escape peaks, in that order.

The observed intensities were in agreement with simulation results obtained with the code PENELOPE, which was then used to simulate the expected behaviour of the TE and QE peaks in gamma-ray detectors with several sizes. It was seen that the TE and QE peaks start being an important detection effect above $\approx$10 MeV and only for large detectors. We developed empirical formulas for the TE/DE intensity dependence on energy and for relating QE/TE with SE/DE ratios, based, respectively, on simulation studies and the physical origin of the phenomenon, to help the identification of these high-order escape peaks in HPGe spectra.

The agreement observed with the simulations, which did not include neither double e^+-e^- pair formation in a single photon interaction nor pair formation by electrons, shows that they are not required to explain the observed TE and QE intensities. These phenomena, however, can play a role and possibly be observed in thin detectors, as already pointed out in [10].

Acknowledgments

To Profs. M.H. Tabacniks, N. Added and the LAMFI technical staff for operating the facility, and Profs. O. Helene and A. Suaide for the help in data analysis. Financial support came from the following agencies and projects: Ministerio de Ciencia e Innovación (PHB2007-0059-TA and FPA2006-12066) and FEDER, Coordenação de Aperfeiçoamento de Pessoal de Nível Superior (CAPES-DGU 176/08), Fundação de Amparo à Pesquisa do Estado de São Paulo (FAPESP), Conselho Nacional de Desenvolvimento Científico e Tecnológico (CNPq), and Comissão Nacional de Energia Nuclear.

References

[1] Y. Jin, R.P. Gardner, K. Verghese, Nucl. Instr. and Meth. A 242 (1986) 416.
[2] M.C. Lee, K. Verghese, R.P. Gardner, Nucl. Instr. and Meth. A 262 (1987) 430.
[3] G.L. Molnar, Z. Revay, T. Belgya, Nucl. Instr. and Meth. A 489 (2002) 140.
[4] S. Raman, C. Yonezawa, H. Matsue, H. Iimur, N. Shinohara, Nucl. Instr. and Meth. A 454 (2000) 389.
[5] H. Utsunomiya, H. Akimune, K. Osaka, T. Kaihori, K. Furutaka, H. Harada, Nucl. Instr. and Meth. A 548 (2005) 455 , doi:10.1016/j.nima.2005.04.062.
[6] H. Harada, et al., Nucl. Instr. and Meth. A 554 (2005) 306, doi:10.1016/j.nima.2005.07.065.
[7] W.A. Metwally, R.P. Gardner, A. Sood, Nucl. Instr. and Meth. B 263 (2007) 50, doi:10.1016/j.nimb.2007.04.137.
[8] N.L. Maidana, D.B. Tridapalli, M.A. Rizzutto, P.R. Pascholati, M.N. Martins, V.R. Vanin, Nucl. Instr. and Meth. A 580 (2007) 106, doi:10.1016/j.nima.2007.05.020.
[9] D.H. Wilkinson, D.E. Alburger, Phys. Rev. C 5 (1972) 719.
[10] N.L. Maidana, et al., Phys. Rev. C 79 (2009) 048501, doi:10.1103/PhysRevC.79.048501.
[11] J. Kramp, et al., Nucl. Phys. A 474 (1987) 412.
[12] D.R. Tilley, H.R. Weller, C.M. Cheves, Nucl. Phys. A 564 (1993) 1.
[13] J.A. Alcántara-Núñez, et al., Nucl. Instr. and Meth. A 497 (2003) 429.
[14] M. Cromaz, T.J.M. Symons, G.J. Lane, I.Y. Lee, R.W. MacLeod, Nucl. Instr. and Meth. A 462 (2001) 519.
[15] W.T. Eadie, et al., Statistical Methods in Experimental Physics, North-Holland, Amsterdam, 1971.
[16] O. Helene, V.R. Vanin, Nucl. Instr. and Meth. A 335 (1993) 227.
[17] F. Salvat, J.M. Fernández-Varea, J. Sempau, PENELOPE–2006: A code System for Monte Carlo Simulation of Electron and Photon Transport, OECD/NEA Data Bank, Issy-les-Moulineaux, 2006, ⟨http://www.nea.fr/lists/penelope.html⟩.
[18] F. Salvat, J.M. Fernández-Varea, Metrologia 46 (2009) S112, doi:10.1088/0026-1394/46/2/S08.
[19] J. Sempau, J.M. Fernández-Varea, E. Acosta, F. Salvat, Nucl. Instr. and Meth. B 207 (2003) 107.
[20] B. Faddegon, et al., Med. Phys. 35 (2009) 4308, doi:10.1118/1.2975150.
[21] R.G. Helmer, J.C. Hardy, V.E. Iacob, M. Sanchez-Vega, R.G. Neilson, J. Nelson, Nucl. Instr. and Meth. A 511 (2003) 360.
[22] A. Ore, J.L. Powell, Phys. Rev. 75 (1949) 1696.
[23] S.C. Pevovar, M.H. Weber, K.G. Lynn, Phys. Stat. Sol. (c) 4 (2007) 3447 , doi:10.1002/pssc.200675786.
[24] T. Kishikawa, S. Noguchi, C. Yonezawa, H. Matsue, A. Nakamura, H. Sawahata, J. Radioanal. Nucl. Chem. 215 (1997) 211.
[25] G.F. Knoll, Radiation Detection and Measurement, third ed., John Wiley & Sons, Hoboken, NJ, 2000.